Dissociative excitation of H_2S by electron impact

S. J. Brotton, E. Vyskocil, W. Kedzierski, and J. W. McConkey
Department of Physics, University of Windsor, Windsor, Ontario, Canada N9B 3P4
(Received 30 January 2009; published 22 April 2009)

Vacuum-ultraviolet emissions following the dissociative excitation of H_2S by electron impact at 100 eV incident energy have been measured. The absolute photoemission cross sections are presented over the wavelength range from 94 to 170 nm and the H, SI, or SII transitions producing the features identified. The measured cross section of the Lyman-α emission at 121.6 nm for an electron-impact energy of 100 eV is $(9.79 \pm 0.67) \times 10^{-18}$ cm^2. Excitation functions of the dominant H and SI emission lines are shown for electron-impact energies from threshold to 300 eV. We study the near-threshold region of the excitation functions and use the measured threshold energies to identify the dominant fragmentation channels.

DOI: 10.1103/PhysRevA.79.042709 PACS number(s): 34.80.Gs, 34.80.Ht, 33.20.Ni

I. INTRODUCTION

Hydrogen sulphide (H_2S) is an important molecule from many standpoints. It is a major pollutant in earth's atmosphere being released in many natural and industrial processes [1–3] and has been identified in comets [4], nebulae [5], interstellar clouds [6], and extragalactic sources [7]. H_2S is also widely used in the semiconductor industry and in plasma processing [8]. The molecule has a relatively large dipole moment of 0.98 D, and so its presence can have a significant effect in plasma situations, for example, on the electrical conductivity. Recent work [9,10] has indicated that H_2S plays an important role in regulating blood pressure in humans.

Electron interactions with H_2S have been studied fairly widely, but there are still significant gaps in our knowledge. The experimental data for the ionization, attachment, total, integral, and momentum-transfer cross sections obtained before 2003 were surveyed in the Landolt-Börnstein review [11], while a broader review covering all the different electron-impact processes was given by Karwasz *et al.* [12]. Measurements of the total cross section cover the range from 1–1000 eV [13–15] and are in good agreement with one another. Elastic differential, integral, and momentum-transfer cross sections have been measured [6] over the energy range from 1 to 30 eV, and a large number of different theoretical approaches have been applied to calculate these parameters (see Refs. [7,8] for summary and discussion). More recently [16,17] both the energy and angular ranges have been extended, and extensive comparisons have been made between experiment and theory. Ionization cross sections have been measured [18–20] from threshold to 1 keV. Agreement between different experiments and between experiment and various semiempirical theories for the ionization cross sections [21,22] is poor. Dissociative attachment resulting in the production of H^-, S^-, and SH^- has been studied by a number of groups [19,20,23–26].

Limited information on excitation or dissociative excitation of H_2S is available. The emission spectrum in the near UV and visible spectral regions, obtained following electron impact, has been presented by Horani *et al.* [27], Dixon *et al.* [28], and Toyoda *et al.* [29]. Prominent features were the H Balmer series and the HS^+ and H_2S^+ molecular emissions. Möhlmann and de Heer [30] measured absolute cross-section data for the Balmer series and obtained a value of 6.2×10^{-18} cm^2 for the Hα line at 100 eV electron-impact energy. Ogawa *et al.* [31] studied the velocity distribution of the excited H(n=4) fragments following dissociation by monitoring the Doppler profile of the Hβ line. Meyer *et al.* [32] investigated the radiative relaxation and fragmentation dynamics of H_2S following excitation by high-energy ($\sim$165 eV) photons by observing fluorescence from H, S^+, S^{2+}, and HS^+ fragments in the 300–700 nm range. To our knowledge, no data are available on emissions in the VUV spectral region.

We present complete coverage of the emissions in the 90–170 nm region and provide excitation functions for prominent transitions and absolute cross-section data. By observing the excitation functions in the near-threshold region, the likely dissociation channels of H_2S following electron-impact excitation are identified.

II. EXPERIMENT

The experimental apparatus has been described in detail elsewhere [33–35], and so only an outline will be presented here. The apparatus consists of an electron-impact collision chamber joined to a $\frac{1}{2}m$ Seya-Namoika VUV spectrometer with a 2400 lines/mm diffraction grating. Base pressures in the two chambers were typically 10^{-7} Torr. To produce an approximately constant electron-beam current over the energy range from 10 to 300 eV, the electron beam was magnetically collimated. The energy resolution of the electron beam was approximately 0.5 eV full width at half maximum (FWHM), although the presence of H_2S was found to degrade this somewhat. Suitable voltages applied to the Faraday cup prevent the backscattering of electrons and allow the efficient collection and recording of the beam current. The beam current was typically 50 μA.

In the cross-beam measurements, a beam of gas molecules effuses from a capillary tube and intersects the electron beam at 90°. The photons emitted at 90° with respect to the electron and gas beams are detected by a channel electron multiplier, which is coated with CsI to increase the detection efficiency at wavelengths above approximately 110 nm. The main advantages of using the cross-beam technique are, first,

the higher concentration of molecules in the interaction region leads to an increased count rate and, second, the adverse effects of the H_2S on the electron-beam energy resolution and filament lifetime are reduced. However, the gas density across the H_2S beam is not uniform and, hence, the interaction volume between the electron beam and target gas can depend on the electron energy through variations in electron-beam focusing. Therefore we checked the reliability of the cross-beam measurements using the static gas method, where a uniform gas density is achieved by removing the capillary tube and then filling the chamber with a homogeneous density of H_2S. The electron-beam current I_e and the driving pressure for the target gas beam P (as measured using a baratron absolute pressure gauge) were recorded synchronously with the photon emission count rate, so that the total photon counts could be normalized with respect to P and I_e. Therefore, any variations in the pressure and current during the data collection did not produce errors in the final data presented below. The H_2S target gas density and the electron-beam current were low enough to prevent resonance self-absorption of emitted radiation and multiple scattering between the electron beam and target gas. Furthermore, the source densities were sufficiently low that radiationless quenching of the excited fragments produced negligible effects.

Two types of experimental data were collected. In the wavelength scans, the electron-beam energy is fixed at 100 eV, while the photon emission rate is measured as a function of wavelength. For the excitation functions, the VUV monochromator system records the photon emission rate of a selected emission line as the electron-beam energy is scanned from threshold to 300 eV. To calibrate the electron-impact energy scale, we collected threshold excitation functions for He($2\ ^1P$-$1\ ^1S$) emission at 58.4 nm and the selected H_2S emission to be calibrated under identical experimental conditions. In particular, the same gas mixture of 100 mTorr of He and 100 mTorr of H_2S was used for both excitation functions. The energy shift required to correct the He($2\ ^1P$-$1\ ^1S$) threshold to the known spectroscopic value was then applied to the H_2S excitation function.

There are a large number of repulsive channels for H_2S, and so any polarization of the photons emitted following dissociative excitation is expected to be small [36]. To our knowledge, a polarization greater than 5% has never been produced by the dissociative excitation of a triatomic molecule. Furthermore, even if the polarization was 5%, the correction to the cross section would be less than 2% [37]. Any possible errors introduced by polarization effects are therefore significantly smaller than the total errors from other sources and thus have been neglected.

III. CALIBRATION OF THE DETECTION EFFICIENCY AS A FUNCTION OF WAVELENGTH

A. Relative detection efficiency

The relative probability of detecting a photon as a function of wavelength was determined by comparing the theoretical H_2 emission spectrum with our corresponding measured spectrum. A similar comparison between experiment and theory was performed by Liu *et al.* [38] over the wavelength range of 114–169 nm and, with slightly improved spectral resolution and theoretical accuracy, by Jonin *et al.* [39] from 90 to 120 nm. This section begins with a review of the established theoretical model. We then discuss our approach to (i) including the effects of resonance self-absorption in the model and (ii) fitting the model to the experimental data.

The photon emission rate, I, following electron-impact excitation of H_2 is the product of the excitation rate g and the emission branching ratio:

$$I(v_j,J_j;v_k,J_k) = g(v_j,J_j)\frac{A(v_j,J_j;v_k,J_k)}{A(v_j,J_j)}, \tag{1}$$

where v and J are the vibrational and rotational quantum numbers, respectively. The subscripts i, j, and k denote the initial H_2 ground state $X\ ^1\Sigma_g^+$; the intermediate $2p\sigma B\ ^1\Sigma_u^+$, $2p\pi C\ ^1\Pi_u$, $3p\sigma B'\ ^1\Sigma_u^+$, and $3p\pi D\ ^1\Pi_u$ excited discrete states; and the final lower state, respectively. $A(v_j,J_j;v_k,J_k)$ is the Einstein coefficient for spontaneous emission of a photon produced by the transition from level j to k. We used the calculated emission probabilities $A(v_j,J_j;v_k,J_k)$ and the observed wave numbers for the B, C, B', and D' emission lines from Refs. [40–43]. $A(v_j,J_j)$ is the total emission probability from level (v_j,J_j) to all possible final states k and includes the discrete states and the continuum, that is,

$$A(v_j,J_j) = \sum_{v_k,J_k} A(v_j,J_j;v_k,J_k) + \sum_{J_k}\int A_c(v_j,J_j;e_k,J_k)de_k. \tag{2}$$

The last term in Eq. (2) is the dissociative transition probability, A_c, of molecular hydrogen into two ground-state $H(1s)$ atoms summed over J_k and integrated over all kinetic energies of the dissociating atoms, e_k. The total transition probabilities for the B, C, B', and D' states of H_2 are calculated in Refs. [44,45].

For one molecule, the total excitation rate from the initial states i to the level (v_j,J_j) is given by

$$g(v_j,J_j) = F_e\sum_i N_i\sigma_{ij}, \tag{3}$$

where F_e is the electron flux, N_i is the probability of the molecule being in the initial state i, and σ_{ij} is the excitation cross section. At a temperature of 300 K, effectively all the H_2 molecules are in the zeroth vibrational state $v_i=0$, and so N_i is the fraction of molecules in the rotational level J_i of the lowest vibrational state, that is,

$$N_i = N(v_i=0,J_i) = \frac{S}{7.398}(2J_i+1)e^{-B_eJ_i(J_i+1)hc/KT}, \tag{4}$$

where $S=1$ or 3 for even or odd J_i, respectively, to account for nuclear-spin statistics, 7.398 is the normalization factor to ensure that $\Sigma_iN_i=1$, and the rotational constant B_e of the H_2 initial state $^1\Sigma_g^+$ is 60.80 cm^{-1}. For an electron-impact energy of 100 eV, in common with other models [38,39], the approximation is made that the electron-impact excitation cross section for optically allowed transitions dominate

those for optically forbidden transitions. For a given excited Σ state in level (v_j,J_j), the summation over i in Eq. (3) then simplifies to adding the excitation rates for the $P(J_i=J_j+1,\ v_i=0,v_j)$ and $R(J_i=J_j-1,\ v_i=0,v_j)$ branches only, whereas for the Π states the $Q(J_i=J_j,\ v_i=0,v_j)$ branch is also included.

The excitation cross section σ_{ij} for an electron-impact energy E and transition energy E_{ij} is calculated using the following function introduced by Shemansky *et al.* [46]:

$$\sigma_{ij} \propto \frac{1}{E_{ij}^3}\frac{1}{E}\frac{(2J_j+1)}{(2J_i+1)}A(v_i,J_i;v_j,J_j)\left[\frac{C_0}{C_7}\left(\frac{1}{X^2}-\frac{1}{X^3}\right)+\sum_{n=1}^{4}(X-1)\exp(-nC_8X)+\frac{C_5}{C_7}+\frac{C_6}{C_7}\frac{1}{X}+\ln X\right], \tag{5}$$

where $X=E/E_{ij}$. We used the values of the coefficients $C_1,\ldots,C_8$ determined by Liu *et al.* [47] from the experimental excitation functions of the Lyman and Werner bands of H_2.

The photons emitted by the decay of the excited H_2 states may be absorbed by the background gas present between the interaction region and the channeltron, which is known as resonance self-absorption. The background H_2 molecules are effectively all in the zeroth vibrational state, and so only emissions resulting from the decay to the $v_k=0$ ground state can be reabsorbed. To account for the effects of resonance self-absorption in the model, the following multiplicative factor is included in Eq. (1):

$$C_{kj}=\int_0^\infty l(\nu-\nu_{kj})\exp\left[-\frac{h\nu_{kj}}{c}B_{kj}N_k l(\nu-\nu_{kj})\alpha\right]d\nu \quad \text{for} \quad v_k=0,$$

$$C_{kj}=1 \quad \text{for} \quad v_k\neq 0, \tag{6}$$

where ν_{kj} denotes the transition frequency, $l(\nu-\nu_{kj})$ is the line profile of the absorption cross section for a given transition $k\rightarrow j$ normalized to unit area, N_k is the fraction of the background molecules in the state k [see Eq. (4)], and α is the column density corresponding to the photon's path,

$$\alpha=\int n(z)dz, \tag{7}$$

with $n(z)$ representing the number density of background H_2 molecules at the spatial position z. B_{kj} is the Einstein transition probability for absorption normalized per unit frequency interval, which can be calculated from the Einstein A_{jk} coefficients [40–43] using the relation

$$B_{kj}=\frac{c^3}{8\pi h\nu_{kj}^3}\frac{2J_j+1}{2J_k+1}A_{jk}. \tag{8}$$

At temperatures around 300 K, the Doppler width is much greater than the natural width of the line. We therefore only include the effects of Doppler broadening on the linewidth, and so $l(\nu-\nu_{kj})$ is represented by a Gaussian centered at $\nu=\nu_{kj}$ with unit area and a FWHM of

$$\Delta\nu_D=\sqrt{2}\frac{2\nu_{kj}}{c}\left(\frac{2kT\ln 2}{M}\right)^{1/2}, \tag{9}$$

where M is the H_2 molecular mass and k is Boltzmann's constant. For self-absorption the Doppler frequency shift occurs in both the emission and absorption processes, and so it is necessary to include the factor of $\sqrt{2}$ in Eq. (9).

The most significant effect of the self-absorption is to reduce the emission intensity for wavelengths shorter than approximately 102 nm, where many of the emission lines involve decay to $v_k=0$. In particular, the emissions from C states with relatively large cross sections decaying to low J_k values are highly attenuated. One approach to reduce the effects of self-absorption is to use relatively low gas pressures. However, a lower gas pressure results in decreased count rates and, hence, much longer collection times are required to achieve an adequate statistical accuracy. We therefore chose to use H_2 gas pressures where the effects of resonance self-absorption are evident and then account for the absorption by treating the column density as an adjustable parameter in the fitting procedure (see below). We obtain a column density α of 6.4×10^{13} cm^{-2}.

In addition to the direct excitation of the discrete states from $i\rightarrow j$, the $E,F\ {}^1\Sigma_g^+$-B cascade effects are included in which excitation occurs from an initial state i to an intermediate excited state such as E or F before decay (or cascade) to the B state. For an electron-impact energy of 100 eV, cascade processes contribute approximately 11% of the total B-state excitation cross section and primarily cause an increase in emissions from B states that decay to final states k with low vibrational quantum numbers v_k [48]. We used the E,F-B cascade model of Ref. [48] and the recommended β value of 0.7.

The excited discrete states can decay to the repulsive ground-state potential curve resulting in two dissociated $H(1s)$ atoms. The decay to the steep potential curve of the ground state from several vibrational levels of the excited state produces a broad continuous emission spectrum. The continuum emission begins at wavelengths above 121.6 nm, but the cross section only becomes significant at longer wavelengths, especially in the region from approximately 145 to 170 nm. For an electron-impact energy of 100 eV, the ratio of the continuum emission cross section to the total emission cross section (including the discrete state and the continuum) is 27.5% for B states and 1.5% for C states [49]. Therefore, only the B-state emission continuum is included in the present model spectrum. The continuum emission rate is calculated using the model discussed in Ref. [49] and the theoretical data available from Ref. [43].

Using Eqs. (1)–(9), we calculated the H_2 emission spectrum produced by the direct excitation of the B, C, B', and D states; $E,F\ {}^1\Sigma_g^+$-B cascade effects, the B-state dissociative continuum; and included the effects of resonance self-absorption. To account for the spectral resolution, the theoretical H_2 emission spectrum is convolved with a Gaussian

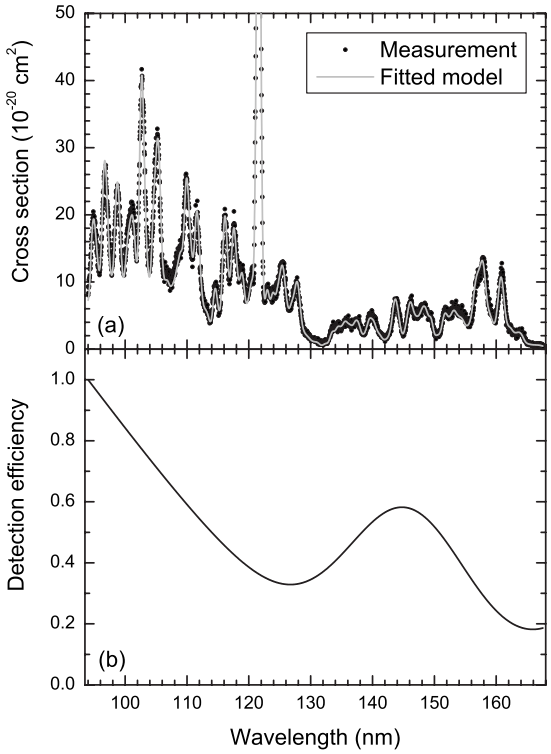

FIG. 1. (a) Fit of the model H_2 emission spectrum to our measured spectrum and (b) the relative probability of detecting a photon as a function of wavelength for the VUV monochromator and channeltron.

apparatus function with a FWHM of 0.79 nm before comparison with experiment.

To determine the variation in the relative probability for detecting a photon with wavelength, we least-squares fitted the following model expression to the measured emission spectrum:

$$P(\lambda;p_1,\ldots,p_M)\left[\mathrm{H}_2(\lambda)+\sum_{m=1}^{3}a_m G(\lambda_{0m},W)\right], \quad (10)$$

where $P(\lambda;p_1,\ldots,p_M)$ is the relative instrumental probability function with adjustable parameters $p_1,\ldots,p_M$, $H_2(\lambda)$ is the broadened theoretical H_2 emission spectrum, and, to represent emissions from the broadened Lyman $H(2p\ ^2P^o)$, $H(3p\ ^2P^o)$, and $H(4p\ ^2P^o)$ Rydberg states, $a_m\ G(\lambda_{0m},W)$ is a Gaussian centered at λ_{0m} with a FWHM of W and an amplitude proportional to a_m. The summation in Eq. (10) is limited to principle quantum numbers $n<5$, since emissions from the Lyman $H(np\ ^2P^o)$ Rydberg states with $n>4$ have relatively small cross sections and merge with the molecular emissions. A suitable function $P(\lambda)$ that reproduces the gradual variations in the detection probability as a function of wavelength with the fewest number of adjustable parameters consists of a cubic polynomial and a Gaussian. In the fitting procedure, the variance is minimized with respect to the parameters $p_1,\ldots,p_M,a_m,\lambda_{0m},W$, and the column density α. The resulting fit and the instrumental probability curve are shown in Fig. 1. The shape of the curve arises from the wavelength dependence of both the channeltron sensitivity and reflection efficiency of the diffraction grating. The broad peak centered at approximately 145 nm is likely because of the variation in the grating reflection efficiency, which is blazed for maximum reflection at a wavelength of 150 nm. The quantum detection efficiency of the channeltron decreases with increasing wavelength over the range shown. An advantage of fitting Eq. (10) to the data is that one can to separate the H Lyman-α peaks for $n<5$ from the overlapping molecular emissions, which improves the accuracy when determining the absolute cross sections by around 6% (see Sec. III B).

We next discuss the main sources of error when determining the probability curve $P(\lambda)$ shown in Fig. 1. First, the accuracy of the theoretical model is partly determined by the errors associated with the coefficients $C_1,\ldots,C_8$ and the transition probabilities $A(v_j,J_j;v_k,J_k)$. For all but the weakest transitions, the fractional errors of the transition probabilities $A(v_j,J_j;v_k,J_k)$ are less than 3%. The transition probabilities $A(v_j,J_j;v_k,J_k)$ occur many times in Eq. (1) and, hence, the individual errors of 3% propagate to give a final error in the photon emission rate I estimated to be less than 10% [39]. For the different excitation energies E_{ij}, the errors in the relative cross sections due to the inaccuracy of the coefficients $C_1,\ldots,C_8$ [see Eq. (1)] are negligible relative to the other errors involved [39]. Second, there are significant emissions from states not included in the present model, namely, the $4p\pi D'\ ^1\Pi_u$ discrete states [39] at wavelengths shorter than approximately 104 nm and, in the region from 92.6 to 95.0 nm, the H($1s$-np) Rydberg series with $n\geq 5$. The errors in the region from 93 to 96 nm are consequently estimated to increase from 10% to less than 15%. Finally, there are statistical errors when fitting the model spectrum to the experimental data. The fitting errors are highest at both ends of the fit, that is, approximately equal to 1% at 94 nm and 3% at 167.5 nm but reduce to less than 1% at intermediate wavelengths. The total error in the probability $P(\lambda)$ is thus approximately 15% in the region from 93 to 96 nm and reduces to around 10% for remainder of the curve.

At wavelengths longer than approximately 170 nm, the H_2 emission cross section becomes small and so the statistical errors in determining the probability curve $P(\lambda)$ are large. As the wavelengths reduce below approximately 94 nm, the cross sections of the states not included in the model become increasingly significant. Therefore we only present below the calibrated cross sections in the wavelength range from 94 to 169 nm.

B. Normalization of the absolute cross sections

To remove the effects of the variation in the detection probability with wavelength, the H_2S wavelength scan is divided by the relative probability function $P(\lambda)$ shown in Fig. 1. The corrected H_2S relative photoemission cross section is placed on an absolute scale by comparison with a known absolute cross section using the relative gas-flow technique (see Van der Burgt *et al.* [37] and references therein). We used the H_2 Lyman-α emission line as the absolute cross-section standard. The cross section for H_2 Lyman-α emission

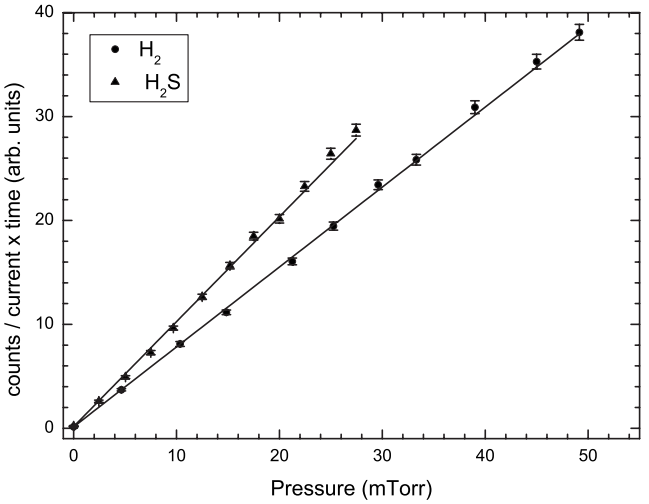

FIG. 2. Photon count rate versus capillary head pressure for H Lyman-α emission from H_2 and H_2S under conditions of molecular flow.

at an electron-impact energy of 100 eV was recently revised by McConkey *et al.* [50] to $(7.03 \pm 0.47) \times 10^{-18}$ cm^2. An ideal H_2S emission feature for comparison is also Lyman-α at 121.6 nm, since it has the same wavelength and the largest cross section in the spectrum.

At sufficiently low pressures, the flow of gas through the single capillary tube is collisionless or "molecular." Under conditions of molecular flow, the number density of target molecules is proportional to the source pressure. Therefore the relative H_2S Lyman-α and H_2 Lyman-α cross sections can be obtained by comparing the slopes of the count rate versus pressure graphs shown in Fig. 2. A capacitance manometer (MKS type 220, 1 Torr full scale range) was used to measure the absolute driving pressure. All the experimental parameters were constant during the measurements including the electron-beam energy, the observed wavelength, and the slit widths. The total photon counts were normalized with respect to the Faraday cup current integrated over the data collection period.

At the spectral resolution of 0.79 nm for the H_2 spectrum, the H Lyman-α emission line appears superimposed on a continuous background from the unresolved molecular emission lines (see Fig. 1). The fitting procedure discussed in Sec. III A allows one to separate accurately the contributions to the cross section by Lyman-α and the molecular emissions. The gradient of the line fitted to the H_2 data shown in Fig. 2 consequently needs to be reduced by 6% before comparison with the H_2S fit. We then obtain

$$\sigma[\mathrm{H_2S(Lyman\text{-}\alpha)}] = (9.79 \pm 0.67) \times 10^{-18}\ \mathrm{cm}^2, \quad (11)$$

where the error is due to the uncertainties in the absolute cross section for H_2 Lyman-α emission and the fitted gradients of the pressure versus count rate graphs. The normalizing factor required to place the H_2S Lyman-α cross section on an absolute scale is applied to the whole H_2S wavelength scan, so that the H_2S features at all observed wavelengths are normalized absolutely.

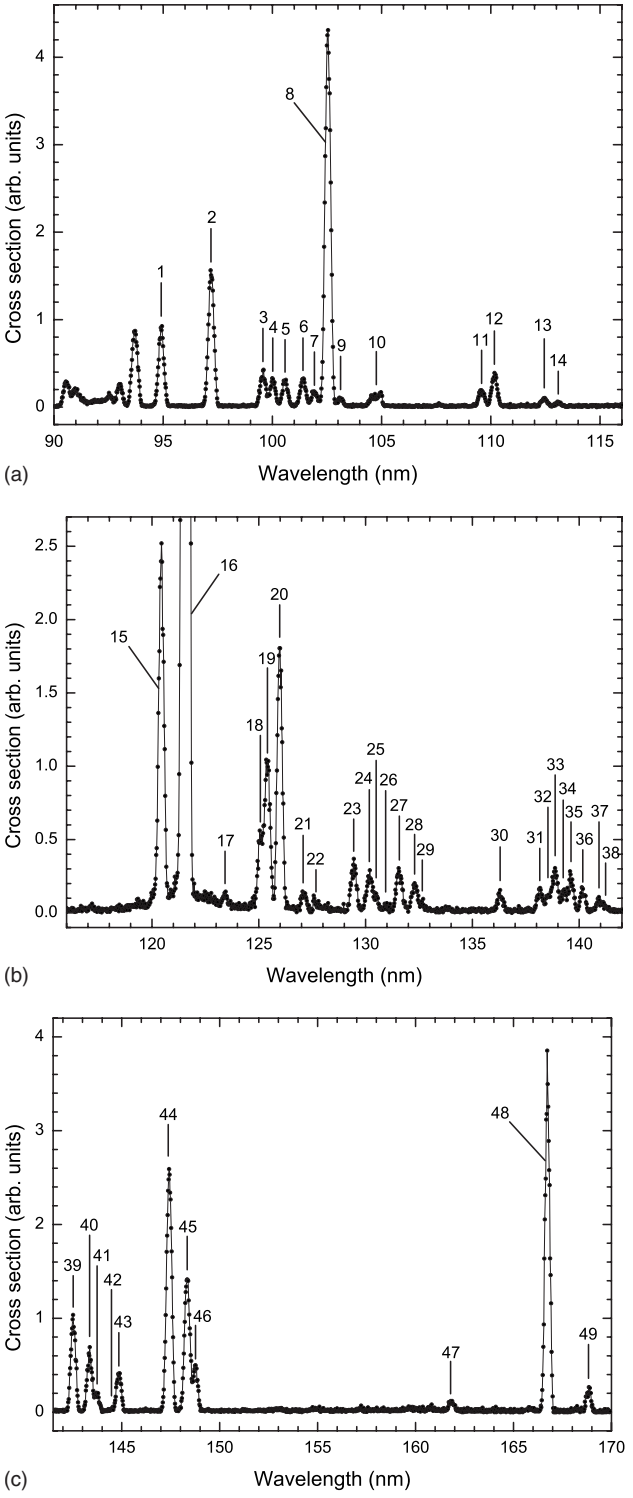

FIG. 3. [(a)–(c)] H_2S photoemission spectrum over the wavelength range from 90 to 170 nm for an electron-impact energy of 100 eV. The cross section has been corrected for the variation in the photon detection probability with wavelength. The transitions producing all but the smallest features are identified in Table I.

IV. RESULTS AND DISCUSSION

A. Spectra

Figures 3(a)–3(c) show the H_2S photoemission spectrum for an electron-impact energy of 100 eV, which has been

corrected for the variation in the detection probability with wavelength. The atom or ion and the transition that produce the features are presented in Table I. At wavelengths below 126 nm, the spectrum is dominated by emissions from S^+ and the H Lyman series, whereas at wavelengths longer than 126 nm the neutral S multiplets are most prominent. The Lyman-α emission at 121.6 nm has much the largest cross section in the spectrum.

To determine the relative cross sections, we fitted Gaussian line shapes to obtain the areas under the peaks shown in Fig. 3. The relative cross sections are then placed on an absolute scale using the method of Sec. III B. The absolute cross sections and the observed wavelengths of the transitions are listed in Table I. The quoted errors in the absolute cross sections include the uncertainties in the areas from the Gaussian fits, the statistical errors when fitting the model spectrum to the experimental data (see Fig. 1), and the uncertainty of 7% when placing the relative cross sections on an absolute scale [see Eq. (11)]. As discussed in Sec. II, any variations in the pressure and current during the data collection do not produce errors after the normalization procedure. In addition to the random experimental errors in Table I, systematic theoretical inaccuracies of 10%–15% in the sensitivity calibration procedure are expected, arising from the inaccuracy of the model H_2 emission spectrum (see Sec. III).

In some regions of the spectrum, weak features overlap with larger peaks and produce shoulders. To improve the fit, Gaussian line shapes were included to model the shoulders, but, due to the low statistical accuracy and nonuniqueness in the fitting procedure (or correlation between the parameters), the weak overlapping features are excluded from Table I. All the features included in the fit are identified by numbers in Figs. 3.

In Fig. 3(c), we note the two prominent SI $[^3D^o\text{-}^3P_{2,1,0}]$ multiplets composed of features numbered 39–41 and 44–46. The former multiplet is produced by dissociation of the parent molecule together with promotion of the outer $3p$ orbital into a $3d$ orbital based on a $^4S^o$ ionic core (see Table I). The multiplet splitting is caused by transitions to the three fine-structure components $^3P_{2,1,0}$ of the ground state. The relative intensities within the multiplet are approximately determined by the statistical weights $(2J_k+1)$ of the ground state. For features 44–46, the $3p$ orbital is excited to a $4s$ level based on a ^2D ionic core. In contrast, the 166.7 nm feature arises from a singlet-singlet transition from the upper $3s^23p^3(^2D)4s\ ^1D^o$ level to the $3s^23p^4\ ^1D_2$ level within the ground configuration.

In addition to the strongest neutral S features discussed above, some of the weaker SI emissions are of interest. Features 31–35 in the wavelength range from 138 to 140 nm [see Fig. 3(b)] represent inner shell $3s \rightarrow 3p$ excitations leading to dipole-allowed transitions within the $3s^23p^4\ ^3P_{2,1,0}\text{-}3s3p^5\ ^3P^o_{2,1,0}$ fine-structure multiplet. The SII features 18–20 produced by the transitions $3s^23p^3\ ^4S^o_{3/2}\text{-}3s3p^4\ ^4P_{1/2,3/2,5/2}$ and feature 15 composed of the four unresolved emissions from the SII $3s^23p^3\ ^2D^o\text{-}3s3p^4\ ^2D$ multiplet also involve inner shell $3s \rightarrow 3p$ excitations. The 168.8 nm $3s^23p^4\ ^1S\text{-}3s3p^5\ ^1P^o$ transition leads to cascade population of the metastable ^1S state within the ground configuration.

In data taken at longer wavelengths than shown in Fig. 3, there is an indication of the SI $[3s^23p^4\ ^3P\text{-}3s^23p^3(^4S)4s\ ^3S^o]$ multiplet between 180.7 and 182.6 nm. However, due to poor sensitivity of the detection system at these wavelengths and the possible contamination of the spectrum by overlapping second order emissions, no positive identification could be made and hence no cross-section data are presented.

B. Excitation functions and dissociation channels

Figure 4 shows the H Lyman-α excitation function produced by the dissociative excitation of H_2S for electron-impact energies from threshold to 300 eV. The curve is relatively featureless with a maximum around 65 eV and a threshold near 13.8 eV. The excitation threshold energies of a given emission line for the different possible fragmentation channels can be calculated using the standard enthalpies of formation, ΔH_f^o, available from, for example, the reaction thermochemistry data page in the NIST Chemistry WebBook [51]. The threshold energies for H(121.6 nm) emission and the corresponding fragmentation channels are given in Table II. The minimum possible energy required to fragment the H_2S molecule into HS+H and excite the H into the $2p$ state is 14.11 eV, which is consistent with our measured threshold within the fitting errors. This dissociative excitation process may be represented by

$$e^-(E) + H_2S(X\ ^1A_1) \rightarrow H(2p) + SH(X\ ^2\Pi) + E_{\rm kin} + e^-(E_s), \tag{12}$$

where X represents the ground state, $E_{\rm kin}$ denotes the kinetic energy of the atomic and molecular fragments, and E_s is the energy of the scattered electron. The emission cross section has a concave upward slope near threshold, which suggests that cascade to $H(2p)$ from atomic $H(n)$ states with $n>2$ enhance the emission cross section. This would be consistent with the findings of Möhlmann and de Heer [30] who studied the excitation of the Balmer series $H(n \rightarrow n=2)$ and measured cross sections with a similar order of magnitude to the Lyman series data presented here. Total fragmentation of the molecule yielding $H(2p)$ with a calculated minimum energy of 17.80 eV (Table II) could also be contributing.

A clear change in slope of the excitation function, which occurs around 28 eV, signals the onset of another $H(2p)$ production process, possibly the simultaneous ionization and excitation channel:

$$e^-(E) + H_2S(X\ ^1A_1) \rightarrow H(2p) + SH^+ + E_{\rm kin} + 2e^-. \tag{13}$$

Process (13) has a calculated minimum onset energy of 24.55 eV, but it is well-known [31,52] that atomic hydrogen fragments from H_2S dissociation can possess considerable kinetic energy due to the repulsive potential surfaces of the excited parent molecule involved. A further possibility, with a predicted minimum energy of 28.0 eV, would be a total fragmentation process with both H atoms excited, namely,

$$e^-(E) + H_2S(X\ ^1A_1) \rightarrow 2H(2p) + S(^3P) + E_{\rm kin} + e^-(E_s). \tag{14}$$

Alternatively, one of the H atoms could remain in the ground state while the S atom is ionized:

TABLE I. The atom or ion and the transition that produce the features numbered in Fig. 3 and the measured emission wavelengths and absolute cross sections.

Feature	Measured peak wavelength (nm)	Measured cross section (10^{-20} cm^2)	Atom or ion	Transition: configurations, terms, and J_i–J_k	NIST wavelength (nm)
1	94.91	26.7 ± 1.9	H	$1s$-$5p$, ^2S-$^2P^o$	94.9743
2	97.19	48.1 ± 3.4	H	$1s$-$4p$, ^2S-$^2P^o$	97.2537
3	99.57	11.49 ± 0.94	SII	$3s^23p^3$-$3s^23p^2(^3P)3d$, $^2D^o$-^2F, $\frac{5}{2}-\frac{7}{2}$	99.6007
4	100.02	8.71 ± 0.78	SII	$3s^23p^3$-$3s^23p^2(^3P)3d$, $^2D^o$-^2F, $\frac{3}{2}-\frac{5}{2}$	100.0485
			SII	$3s^23p^3$-$3s^23p^2(^3P)3d$, $^2D^o$-^2F, $\frac{5}{2}-\frac{5}{2}$	100.0804
5	100.58	8.75 ± 0.74	SII	$3s^23p^3$-$3s^23p^2(^3P)3d$, $^2D^o$-^4D, $\frac{5}{2}-\frac{7}{2}$	100.6093
			SII	$3s^23p^3$-$3s^23p^2(^3P)3d$, $^2D^o$-^4D, $\frac{3}{2}-\frac{5}{2}$	100.6261
6	101.40	9.54 ± 0.80	SII	$3s^23p^3$-$3s^23p^2(^3P)4s$, $^2D^o$-^2P, $\frac{3}{2}-\frac{3}{2}$	101.4119
			SII	$3s^23p^3$-$3s^23p^2(^3P)4s$, $^2D^o$-^2P, $\frac{5}{2}-\frac{3}{2}$	101.4449
7	101.92	5.27 ± 0.55	SII	$3s^23p^3$-$3s^23p^2(^3P)4s$, $^2D^o$-^2P, $\frac{3}{2}-\frac{1}{2}$	101.9537
8	102.54	133.4 ± 9.1	H	$1s$-$3p$, ^2S-$^2P^o$	102.5722
9	103.12	2.29 ± 0.31	SII	$3s^23p^3$-$3s^23p^2(^1D)4s$, $^2P^o$-^2D, $\frac{1}{2}-\frac{3}{2}$	103.0890
			SII	$3s^23p^3$-$3s^23p^2(^1D)4s$, $^2P^o$-^2D, $\frac{3}{2}-\frac{5}{2}$	103.1375
11	109.58	5.71 ± 0.53	SII	$3s^23p^3$-$3s^23p^2(^3P)3d$, $^2D^o$-^2P, $\frac{3}{2}-\frac{1}{2}$	109.6602
12	110.17	10.96 ± 0.87	SII	$3s^23p^3$-$3s^23p^2(^3P)3d$, $^2D^o$-^2P, $\frac{3}{2}-\frac{3}{2}$	110.1975
			SII	$3s^23p^3$-$3s^23p^2(^3P)3d$, $^2D^o$-^2P, $\frac{5}{2}-\frac{3}{2}$	110.2360
13	112.44	2.86 ± 0.33	SII	$3s^23p^3$-$3s^23p^2(^3P)4s$, $^2P^o$-^2P, $\frac{1}{2}-\frac{3}{2}$	112.4396
			SII	$3s^23p^3$-$3s^23p^2(^3P)4s$, $^2P^o$-^2P, $\frac{3}{2}-\frac{3}{2}$	112.4978
14	113.09	1.20 ± 0.22	SII	$3s^23p^3$-$3s^23p^2(^3P)4s$, $^2P^o$-^2P, $\frac{1}{2}-\frac{1}{2}$	113.1052
			SII	$3s^23p^3$-$3s^23p^2(^3P)4s$, $^2P^o$-^2P, $\frac{3}{2}-\frac{1}{2}$	113.1658
15	120.43	69.9 ± 6.5	SII	$3s^23p^3$-$3s3p^4$, $^2D^o$-^2D, $\frac{3}{2}-\frac{5}{2}$	120.3861
			SII	$3s^23p^3$-$3s3p^4$, $^2D^o$-^2D, $\frac{3}{2}-\frac{3}{2}$	120.4290
			SII	$3s^23p^3$-$3s3p^4$, $^2D^o$-^2D, $\frac{5}{2}-\frac{5}{2}$	120.4335
			SII	$3s^23p^3$-$3s3p^4$, $^2D^o$-^2D, $\frac{5}{2}-\frac{3}{2}$	120.4735
16	121.57	979 ± 67	H	$1s$-$2p$, ^2S-$^2P^o$, $\frac{1}{2}-\frac{3}{2}$	121.567
18	125.07	14.2 ± 1.7	SII	$3s^23p^3$-$3s3p^4$, $^4S^o$-^4P, $\frac{3}{2}-\frac{1}{2}$	125.0578
19	125.40	30.5 ± 2.7	SII	$3s^23p^3$-$3s3p^4$, $^4S^o$-^4P, $\frac{3}{2}-\frac{3}{2}$	125.3805
20	125.98	50.6 ± 3.7	SII	$3s^23p^3$-$3s3p^4$, $^4S^o$-^4P, $\frac{3}{2}-\frac{5}{2}$	125.9518
23	129.44	9.75 ± 0.85	SI	$3s^23p^4$-$3s^23p^3(^2P^o)4s$, ^3P-$^3P^o$, 2–2	129.565 26
			SI	$3s^23p^4$-$3s^23p^3(^2P^o)4s$, ^3P-$^3P^o$, 2–1	129.617 38
24	130.17	7.92 ± 0.87	SI	$3s^23p^4$-$3s^23p^3(^2P^o)4s$, ^3P-$^3P^o$, 1–2	130.233 70
			SI	$3s^23p^4$-$3s^23p^3(^2P^o)4s$, ^3P-$^3P^o$, 1–1	130.286 33
			SI	$3s^23p^4$-$3s^23p^3(^2P^o)4s$, ^3P-$^3P^o$, 1–0	130.311 05
			SI	$3s^23p^4$-$3s^23p^3(^4S^o)6s$, ^3P-$^3S^o$, 2–1	130.342 95
27	131.58	8.99 ± 0.81	SI	$3s^23p^4$-$3s^23p^3(^4S^o)4d$, ^3P-$^3D^o$, 2–3	131.654 23
			SI	$3s^23p^4$-$3s^23p^3(^4S^o)4d$, ^3P-$^3D^o$, 2–2	131.661 83
			SI	$3s^23p^4$-$3s^23p^3(^4S^o)4d$, ^3P-$^3D^o$, 2–1	131.661 83
28	132.29	5.62 ± 0.63	SI	$3s^23p^4$-$3s^23p^3(^4S^o)4d$, ^3P-$^3D^o$, 1–2	132.351 53
			SI	$3s^23p^4$-$3s^23p^3(^4S^o)4d$, ^3P-$^3D^o$, 1–1	132.352 20
30	136.30	3.33 ± 0.40	SI	$3s^23p^4$-$3s^23p^3(^2P^o)5s$, ^1S-$^1P^o$, 0–1	136.130 40
			SI	$3s^23p^4$-$3s^23p^3(^2D^o)3d$, ^1D-$^1F^o$, 2–3	136.303 30
			SII	$3s^23p^3$-$3s3p^4$, $^2P^o$-^2D, $\frac{1}{2}-\frac{3}{2}$	136.3011
			SII	$3s^23p^3$-$3s3p^4$, $^2P^o$-^2D, $\frac{3}{2}-\frac{5}{2}$	136.3384
			SII	$3s^23p^3$-$3s3p^4$, $^2P^o$-^2D, $\frac{3}{2}-\frac{3}{2}$	136.3902
31	138.15	4.21 ± 0.48	SI	$3s^23p^4$-$3s3p^5$, ^3P-$^3P^o$, 2–1	138.155 21

TABLE I. (*Continued.*)

Feature	Measured peak wavelength (nm)	Measured cross section (10^{-20} cm^2)	Atom or ion	Transition: configurations, terms, and J_i–J_k	NIST wavelength (nm)
32	138.53	2.80 ± 0.39	SI	$3s^2 3p^4$-$3s 3p^5$, ^3P-$^3P^o$, 1–0	138.551 00
33	138.87	8.7 ± 1.0	SI	$3s^2 3p^4$-$3s 3p^5$, ^3P-$^3P^o$, 2–2	138.843 47
			SII	$3s^2 3p^4$-$3s 3p^5$, ^3P-$^3P^o$, 1–1	138.915 38
34	139.29	3.24 ± 0.61	SI	$3s^2 3p^4$-$3s 3p^5$, ^3P-$^3P^o$, 0–1	139.258 78
35	139.62	6.45 ± 0.68	SI	$3s^2 3p^4$-$3s 3p^5$, ^3P-$^3P^o$, 1–2	139.611 22
36	140.16	3.95 ± 0.33	SI	$3s^2 3p^4$-$3s^2 3p^3(^4S^o)5s$, ^3P-$^3S^o$, 2–1	140.151 36
37	140.93	2.24 ± 0.40	SI	$3s^2 3p^4$-$3s^2 3p^3(^4S^o)5s$, ^3P-$^3S^o$, 1–1	140.933 69
39	142.52	29.6 ± 2.1	SI	$3s^2 3p^4$-$3s^2 3p^3(^4S^o)3d$, ^3P-$^3D^o$, 2–3	142.503 01
			SI	$3s^2 3p^4$-$3s^2 3p^3(^4S^o)3d$, ^3P-$^3D^o$, 2–2	142.5188
			SI	$3s^2 3p^4$-$3s^2 3p^3(^4S^o)3d$, ^3P-$^3D^o$, 2–1	142.521 90
40	143.36	19.1 ± 1.5	SI	$3s^2 3p^4$-$3s^2 3p^3(^4S^o)3d$, ^3P-$^3D^o$, 1–2	143.3278
			SI	$3s^2 3p^4$-$3s^2 3p^3(^4S^o)3d$, ^3P-$^3D^o$, 1–1	143.331 05
41	143.75	4.62 ± 0.53	SI	$3s^2 3p^4$-$3s^2 3p^3(^4S^o)3d$, ^3P-$^3D^o$, 0–1	143.696 75
43	144.85	11.91 ± 0.98	SI	$3s^2 3p^4$-$3s^2 3p^3(^2P^o)4s$, ^1D-$^1P^o$, 2–1	144.822 90
44	147.42	82.6 ± 5.7	SI	$3s^2 3p^4$-$3s^2 3p^3(^2D^o)4s$, ^3P-$^3D^o$, 2–3	147.399 48
			SI	$3s^2 3p^4$-$3s^2 3p^3(^2D^o)4s$, ^3P-$^3D^o$, 2–2	147.438 00
			SI	$3s^2 3p^4$-$3s^2 3p^3(^2D^o)4s$, ^3P-$^3D^o$, 2–1	147.457 15
45	148.34	47.8 ± 3.4	SI	$3s^2 3p^4$-$3s^2 3p^3(^2D^o)4s$, ^3P-$^3D^o$, 1–2	148.303 90
			SI	$3s^2 3p^4$-$3s^2 3p^3(^2D^o)4s$, ^3P-$^3D^o$, 1–1	148.323 30
			SI	$3s^2 3p^4$-$3s^2 3p^3(^4S^o)3d$, ^3P-$^5D^o$, 0–1	148.5622
46	148.77	12.7 ± 1.1	SI	$3s^2 3p^4$-$3s^2 3p^3(^2D^o)4s$, ^3P-$^3D^o$, 0–1	148.715 00
47	161.83	3.19 ± 0.41		No corresponding emission line in the NIST tables	
48	166.73	106.4 ± 7.3	SI	$3s^2 3p^4$-$3s^2 3p^3(^2D^o)4s$, ^1D-$^1D^o$, 2–2	166.668 75
49	168.84	6.77 ± 0.62	SI	$3s^2 3p^4$-$3s^2 3p^3(^2D^o)3d$, ^1S-$^1P^o$, 0–1	168.753 05

$$e^-(E) + H_2S(X\ ^1A_1) \rightarrow H(1s) + H(2p) + S^+(X) + E_{kin} + 2e^-. \quad (15)$$

Our data do not extend to a high enough energy to make a reliable Bethe plot of σE versus ln E, which would indicate whether the initial excitation of the parent molecule was optically allowed or forbidden. However, Möhlmann and de Heer's [30] Balmer emission cross section data, following electron impact on H_2S, indicates that the initial excitation of the parent molecule exhibits the characteristics of a spin allowed but optically forbidden transition. It is reasonable to assume that our H(n=2) excitation is similar.

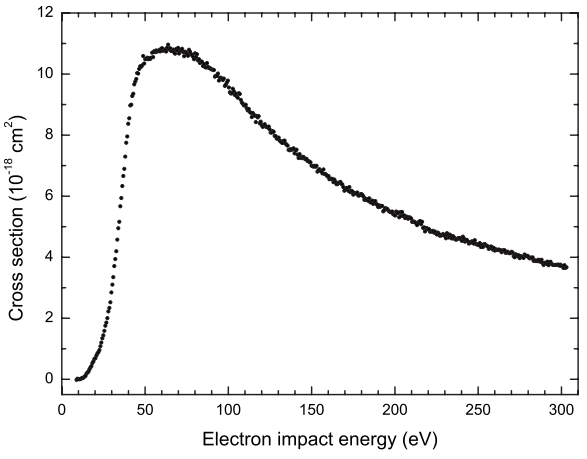

FIG. 4. H(121.6 nm) excitation function for electron-impact energies from threshold to 300 eV. See feature 16 in Table I for the transition details.

TABLE II. Calculated minimum threshold energies in eV for H(121.6 nm) emission for selected fragmentation channels below an impact energy of 40 eV.

Fragmentation channel	H(121.6 nm)
$H(2p)+HS^-(X)$	11.83
$H(2p)+HS(X)$	14.12
$H(2p)+H(X)+S(X)$	17.80
$H(2p)+HS^+(X)$	24.55
$2H(2p)+S(X)$	28.00
$H(2p)+H(X)+S^+(X)$	28.16
$H(2p)+H^+ + S(X)$	31.40
$2H(2p)+S^+(X)$	38.36

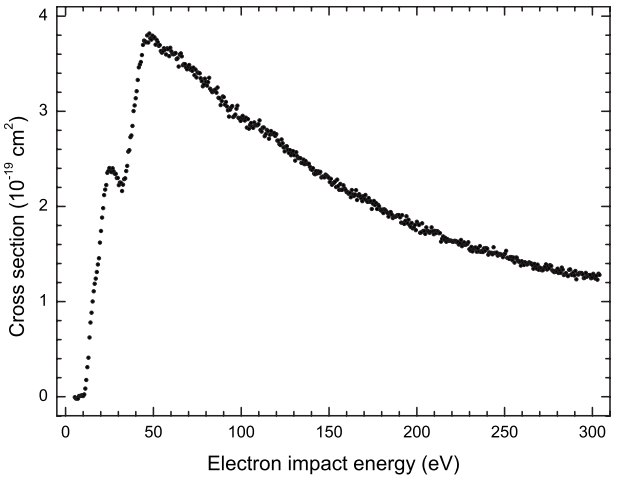

FIG. 5. SI(142.5 nm) excitation function for electron-impact energies from threshold to 300 eV. See feature 39 in Table I for the transition details.

Figures 5–7 show excitation functions for three prominent neutral S lines at 142.5, 147.4, and 166.7 nm. In Fig. 8, the H(121.6 nm), S(142.5 nm), S(147.4 nm), S(166.7 nm), and He(58.4 nm) excitation functions are compared in the near-threshold region. The calculated minimum threshold energies for S(142.5 nm), S(147.4 nm), and S(166.7 nm) emissions for the different possible fragmentation channels are presented in Table III.

It is clear from Figs. 5–7 and the more detailed observation of the near-threshold region shown in Fig. 8 that the three excitation functions have many common features. First, by fitting a straight line in the threshold region ($E<18$ eV) convolved with a Gaussian to represent the energy spread of the electron beam, we determined the following similar threshold energies E_t:

$$E_t[\mathrm{S}(142.5\ \mathrm{nm})] = 11.54 \pm 0.37\ \mathrm{eV},$$

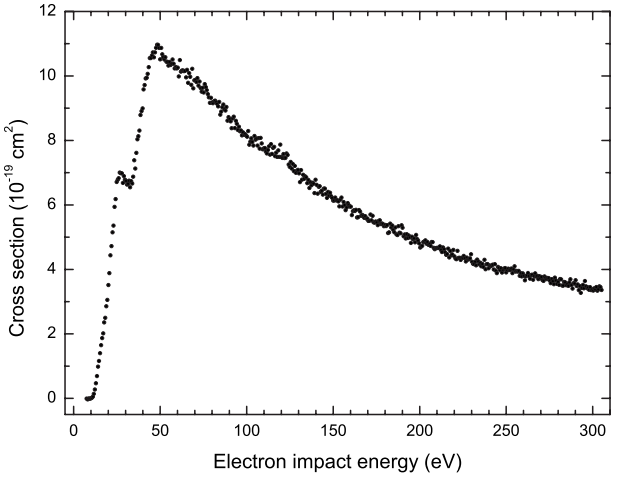

FIG. 6. SI(147.4 nm) excitation function for electron-impact energies from threshold to 300 eV. See feature 44 in Table I for the transition details.

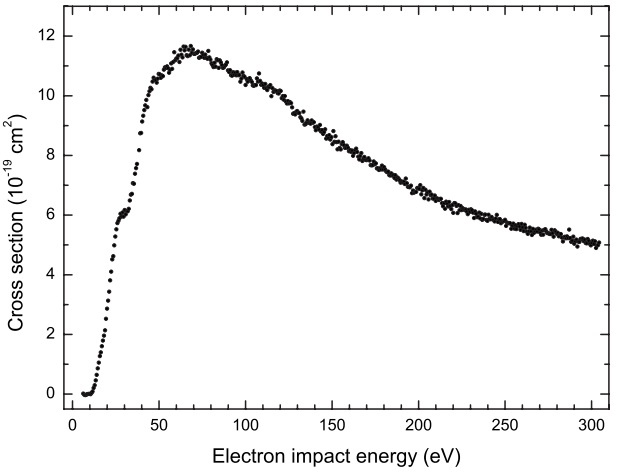

FIG. 7. SI(166.7 nm) excitation function for electron-impact energies from threshold to 300 eV. See feature 48 in Table I for the transition details.

$$E_t[\mathrm{S}(147.4\ \mathrm{nm})] = 11.66 \pm 0.33\ \mathrm{eV},$$

$$E_t[\mathrm{S}(166.7\ \mathrm{nm})] = 12.17 \pm 0.37\ \mathrm{eV}. \quad (16)$$

To determine the process responsible for the energies [Eq. (16)], consider the fragmentation channels:

$$e^-(E) + \mathrm{H_2S}(X\ ^1A_1) \rightarrow \mathrm{S}^* + \mathrm{H_2}(X,v) + E_{\mathrm{kin}} + e^-(E_s), \quad (17)$$

where S^* denotes the excited states $S[3s^2 3p^3(^4S^o)3d\ ^3D^o]$, $S[3s^2 3p^3(^2D^o)4s\ ^3D^o]$, or $S[3s^2 3p^3(^2D^o)4s\ ^1P^o]$; and the H_2 molecule may be left in the vibrationally excited state v. An energy of 3.09 eV [51] is required to separate the S atom from the parent molecule to form $S+H_2$ and an additional 8.69, 8.41, or 8.58 eV is needed to produce the S(142.5 nm), S(147.4 nm), and S(166.7 nm) emissions, respectively. The threshold energies for processes (17) are therefore 11.78,

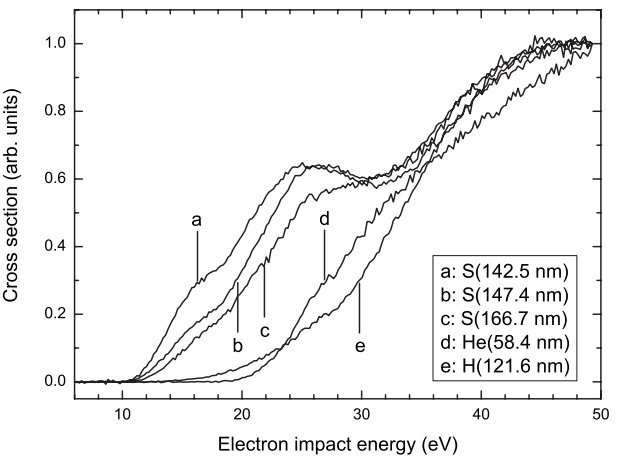

FIG. 8. H(121.6 nm), SI(142.5 nm), SI(147.4 nm), SI(166.7 nm), and He(58.4 nm) excitation functions in the near-threshold region.

TABLE III. Calculated minimum threshold energies in eV for S(142.5 nm), S(147.4 nm), and S(166.7 nm) emissions for selected fragmentation channels below an impact energy of 40 eV.

Fragmentation channel	S(142.5 nm)	S(147.4 nm)	S(166.7 nm)
$S^*+H_2(X)$	11.79	11.50	11.67
$S^*+H(X)+H(X)$	16.30	16.02	16.19
$S^*+H(X)+H(2p)$	26.50	26.21	26.39
$S^*+H_2^+$	27.22	26.93	27.10
$S^*+H(X)+H^+$	29.90	29.61	29.79
$S^*+2H(2p)$	36.70	36.41	36.59

11.50, and 11.67 eV (see Table III), which are consistent with our measured onsets [Eq. (16)] within the experimental errors. As Table III shows, only processes (17) could therefore produce our measured threshold energies.

A second common feature is the clear change of slope in the excitation functions at around 18–19 eV. The most likely cause is the onset of total fragmentation of the parent molecule with excitation of the S fragment. Thus:

$$e^-(E) + H_2S(X\ ^1A_1) \rightarrow S^* + 2H(X) + E_{\text{kin}} + e^-(E_s). \tag{18}$$

The predicted minimum energies [51] for processes (18) range from 16.0 to 16.3 eV depending on which S emission is excited (see Table III). The differences of 2–3 eV between the observed and predicted thresholds would be taken up as kinetic energy of the atomic fragments. Such fragment kinetic energies are reasonable [31,52].

A third common feature of the S excitation functions is a sharp onset near 31 eV. This is most probably due to total fragmentation of the H_2S molecule with simultaneous excitation or ionization of one of the H atoms in addition to S excitation, that is,

$$e^-(E) + H_2S(X\ ^1A_1) \rightarrow S^* + H(np) + H(X) + E_{\text{kin}} + e^-(E_s),$$
$$E_t = 26.2 - 26.5\ \text{eV}, \tag{19}$$

$$e^-(E) + H_2S(X\ ^1A_1) \rightarrow S^* + H^+ + H(X) + E_{\text{kin}} + 2e^-,$$
$$E_t = 29.6 - 29.9\ \text{eV}, \tag{20}$$

where $n=2$ and the range of threshold energies, E_t, for the different S excitations are shown. In addition, there are a series of possible thresholds at energies between processes (19) and (20) due to the H(np) Rydberg states with $n>2$. The calculated thresholds for processes (19) and (20) are lower than the observed values but, again, it is expected that the relevant repulsive surfaces will be quite steep resulting in considerable fragment kinetic energies, particularly of the H fragments. The partial cross section for the production of H^+ is significantly larger than that for H_2^+ [19]. Therefore, emissions from fragmentation channel [Eq. (20)], $S^*+H^+ + H(X)$, are expected to dominate those from $S^*+H_2^+$ (see Table III).

The S(166.7 nm) excitation function (Fig. 7) exhibits, first, a less rapid rise from threshold to the maximum cross section and, second, a slower fall off as the energy increases above approximately 65 eV than the S(142.5 nm) or S(147.4 nm) excitation functions (Figs. 5 and 6). This suggests that the initial excitation of the parent molecule leading to S(166.7 nm) emission has a larger optically allowed component than for the S(142.5 nm) or S(147.4 nm) emissions.

Our measured H($1s$-$3p$) cross section (see Table I) can be used to calculate the H($2s$-$3p$) cross section at 100 eV incident energy. Using the theoretical H($3p$-$1s$)/H($3p$-$2s$) branching ratio of 7.448 [53], we obtain a cross section σ[H($2s$-$3p$)] of 0.17×10^{-18} cm^2 for the two transitions $^2S_{1/2}$-$^2P_{1/2,3/2}$ within the Balmer-α multiplet. Möhlmann and de Heer [30] measured a total cross section σ_t (Balmer-α) of 6.2×10^{-18} cm^2 at the same electron-impact energy for all seven unresolved transitions contributing to the Balmer-α multiplet. The ratio of σ[H($2s$-$3p$)]/σ_t(Balmer-α) at under 3% would require that most of the Balmer-α excitation is via the $3s$ and $3d$ states.

Using the SII data from Table I, we find that our total excited S^+ ion production for 100 eV incident energy in the wavelength range from 94 to 130 nm is 2.25×10^{-18} cm^2. This is just 2.6% of the total cross section for S^+ production of 85.2×10^{-18} cm^2 at 100 eV measured by Rao and Srivastava [19].

V. CONCLUSION

We have studied the VUV radiation produced following the dissociative excitation of H_2S by electron impact at 100 eV incident energy. The relative sensitivity with wavelength of the VUV monochromator system was calibrated by comparing our measured H_2 emission spectrum with the corresponding theoretical cross section. The relative photoemission cross sections were placed on an absolute scale using the relative gas-flow technique and the H_2 Lyman-α emission line as the absolute cross-section standard. The absolute photoemission cross sections were presented over the wavelength range from 94 to 170 nm and the H, SI, or SII transitions producing the features identified. Excitation functions for electron-impact energies from threshold to 300 eV were shown for selected SI and H emissions with the largest cross sections. By examining the near-threshold region of the excitation functions, we determined the threshold energies for the dominant fragmentation channels of the dissociating H_2S molecule. We identified the processes likely responsible for each threshold by comparing the measured threshold energies with the values calculated using thermochemical data.

ACKNOWLEDGMENTS

Financial support for this work from the Natural Sciences and Engineering Research Council of Canada is gratefully acknowledged. Expert technical help was obtained from the University of Windsor, Physics Department mechanical and electronic shops. Dr. H. Abgrall kindly supplied tabular data for the H_2 model spectrum used in the calibration of the detector sensitivity with wavelength.

[1] N. D. Sze and M. K. W. Ko, Atmos. Environ. **14**, 1223 (1980).
[2] D. Rolle, H. Kalfa, and H. E. Buhler, Werkst. Korros. **44**, 1 (1993).
[3] T. S. Bates, B. K. Lamb, A. Guenther, J. Dignon, and R. E. Stoiber, J. Atmos. Chem. **14**, 315 (1992).
[4] D. Bockelée-Morvan, J. Crovisier, M. J. Mumma, and H. A. Weaver, in *Comets II*, edited by M. C. Festou, H. Uwe Keller, and H. A. Weaver (University of Arizona Press, Tucson, 2004), p. 391.
[5] Y. C. Minh, L. M. Ziurys, W. M. Irvine, and D. McGonagle, Astrophys. J. **360**, 136 (1990).
[6] R. J. Gulley, M. J. Brunger, and S. J. Buckman, J. Phys. B **26**, 2913 (1993).
[7] M. Gupta and K. L. Baluja, Eur. Phys. J. D **41**, 475 (2007).
[8] P. Rawat, I. Iga, M.-T. Lee, L. M. Brescansin, M. G. P. Homem, and L. E. Machado, Phys. Rev. A **68**, 052711 (2003).
[9] J.-S. Bian, Q. C. Yong, T.-T. Pan, Z.-N. Feng, M. Y. Ali, S. Zhou, and P. K. Moore, J. Pharmacol. Exp. Ther. **316**, 670 (2005).
[10] D. J. Lefer, Proc. Natl. Acad. Sci. U.S.A. **104**, 17907 (2007).
[11] Y. Itikawa, *Photon and Electron Interactions with Atoms, Molecules, and Ions*, Landolt-Börnstein, New Series, Group I, Vol. 17 (Springer, New York, 2003), Pt. C.
[12] G. P. Karwasz, R. S. Brusa, and A. Zecca, Riv. Nuovo Cimento **24**, 1 (2001).
[13] C. Szmytkowski and K. Maciag, Chem. Phys. Lett. **129**, 321 (1986).
[14] A. Zecca, G. P. Karwasz, and R. S. Brusa, Phys. Rev. A **45**, 2777 (1992).
[15] C. Szmytkowski, P. Mozejko, and A. Krzysztofowicz, Radiat. Phys. Chem. **68**, 307 (2003).
[16] H. Cho, S. J. Park, and Y. S. Park, J. Korean Phys. Soc. **46**, 431 (2005).
[17] L. M. Brescansin, L. E. Machado, M.-T. Lee, H. Cho, and Y. S. Park, J. Phys. B **41**, 185201 (2008).
[18] B. G. Lindsay, R. Rejoub, and R. F. Stebbings, J. Chem. Phys. **118**, 5894 (2003).
[19] M. V. V. S. Rao and S. K. Srivastava, J. Geophys. Res., [Planets] **98**, 13137 (1993).
[20] D. S. Belic and M. V. Kurepa, Fizika (Zagreb) **17**, 117 (1985).
[21] Y.-K. Kim, W. Hwang, N. M. Weinberger, M. A. Ali, and M. E. Rudd, J. Chem. Phys. **106**, 1026 (1997).
[22] S. P. Khare and W. J. Meath, J. Phys. B **20**, 2101 (1987).
[23] R. Azria, M. Tronc, and S. Goursaud, J. Chem. Phys. **56**, 4234 (1972).
[24] R. Azria, Y. Le Coat, G. Lefevre, and D. Simon, J. Phys. B **12**, 679 (1979).
[25] M. Tronc, S. Goursaud, R. Azria, and F. Fiquet-Fayard, J. Phys. **34**, 381 (1973).
[26] R. Abouaf and D. Teillet-Billy, Int. J. Mass Spectrom. **277**, 79 (2008).
[27] M. Horani, S. Leach, and J. Rostas, J. Mol. Spectrosc. **23**, 115 (1967).
[28] R. N. Dixon, G. Duxbury, J. Rostas, and M. Horani, Mol. Phys. **22**, 977 (1971).
[29] M. Toyoda, T. Ogawa, and N. Ishibashi, Bull. Chem. Soc. Jpn. **47**, 95 (1974).
[30] G. R. Möhlmann and F. J. de Heer, Chem. Phys. **40**, 157 (1979).
[31] T. Ogawa, M. Tsukada, and K. Nakashima, Chem. Phys. **156**, 473 (1991).
[32] M. Meyer, P. O'Keeffe, J. Plenge, R. Flesch, and E. Rühl, J. Chem. Phys. **125**, 214306 (2006).
[33] W. Kedzierski, A. Abdellatif, J. W. McConkey, K. Bartschat, D. V. Fursa, and I. Bray, J. Phys. B **34**, 3367 (2001).
[34] S. Wang and J. W. McConkey, J. Phys. B **25**, 5461 (1992).
[35] J. L. Forand, S. Wang, J. M. Woolsey, and J. W. McConkey, Can. J. Phys. **66**, 349 (1988).
[36] R. J. Van Brunt and R. N. Zare, J. Chem. Phys. **48**, 4304 (1968).
[37] P. J. M. van der Burgt, W. B. Westerveld, and J. S. Risley, J. Phys. Chem. Ref. Data **18**, 1757 (1989).
[38] X. Liu, S. M. Ahmed, R. A. Multari, G. K. James, and J. M. Ajello, Astrophys. J., Suppl. Ser. **101**, 375 (1995).
[39] C. Jonin, X. Liu, J. M. Ajello, G. K. James, and H. Abgrall, Astrophys. J., Suppl. Ser. **129**, 247 (2000).
[40] H. Abgrall, E. Roueff, F. Launay, J.-Y. Roncin, and J.-L. Subtil, Astron. Astrophys. Suppl. Ser. **101**, 273 (1993).
[41] H. Abgrall, E. Roueff, F. Launay, J.-Y. Roncin, and J.-L. Subtil, Astron. Astrophys. Suppl. Ser. **101**, 323 (1993).
[42] H. Abgrall, E. Roueff, F. Launay, and J.-Y. Roncin, Can. J. Phys. **72**, 856 (1994).
[43] MOLAT—Atomic and Molecular Data (http://molat.obspm.fr).
[44] H. Abgrall, E. Roueff, and I. Drira, Astron. Astrophys. Suppl. Ser. **141**, 297 (2000).
[45] CDS database (http://cdsweb.u-strasbg.fr).
[46] D. E. Shemansky, J. M. Ajello, D. T. Hall, and B. Franklin, Astrophys. J. **296**, 774 (1985).
[47] X. Liu, D. E. Shemansky, S. M. Ahmed, G. K. James, and J. M. Ajello, J. Geophys. Res., [Space Phys.] **103**, 26739 (1998).
[48] H. Abgrall, E. Roueff, X. Liu, D. E. Shemansky, and G. K. James, J. Phys. B **32**, 3813 (1999).
[49] H. Abgrall, E. Roueff, X. Liu, and D. E. Shemansky, Astrophys. J. **481**, 557 (1997).
[50] J. W. McConkey, C. P. Malone, P. V. Johnson, C. Winstead, V. McKoy, and I. Kanik, Phys. Rep. **466**, 1 (2008).
[51] NIST Chemistry WebBook, NIST Standard Reference Database No. 69, edited by P. J. Linstrom and W. G. Mallard, June 2005, National Institute of Standards and Technology, Gaithersburg MD, 20899 (http://webbook.nist.gov).
[52] N. Kouchi, M. Ohno, K. Ito, N. Oda, and Y. Hatano, *Proceedings of the Eleventh ICPEAC, Kyoto*, 1979, p. 366.
[53] NIST Atomic Spectra Database, URL: http://physics.nist.gov (National Institute of Standards and Technology, Gaithersburg, MD).